



HAL
open science

High-Throughput Computing Guided Low/High Index Optical Coupling Layer for Record-Performance Semitransparent Organic Solar Cells

Tao Xu, Baozhong Deng, Yanglin Zhao, Zihan Wang, Gaëtan Lévêque, Yannick Lambert, Bruno Grandidier, Shenghao Wang, Furong Zhu

► **To cite this version:**

Tao Xu, Baozhong Deng, Yanglin Zhao, Zihan Wang, Gaëtan Lévêque, et al.. High-Throughput Computing Guided Low/High Index Optical Coupling Layer for Record-Performance Semitransparent Organic Solar Cells. *Advanced Energy Materials*, 2023, 13 (35), 10.1002/aenm.202301367 . hal-04182429

HAL Id: hal-04182429

<https://hal.science/hal-04182429>

Submitted on 17 Aug 2023

HAL is a multi-disciplinary open access archive for the deposit and dissemination of scientific research documents, whether they are published or not. The documents may come from teaching and research institutions in France or abroad, or from public or private research centers.

L'archive ouverte pluridisciplinaire **HAL**, est destinée au dépôt et à la diffusion de documents scientifiques de niveau recherche, publiés ou non, émanant des établissements d'enseignement et de recherche français ou étrangers, des laboratoires publics ou privés.



Distributed under a Creative Commons Attribution 4.0 International License

High-Throughput Computing Guided Low/High Index Optical Coupling Layer for Record-Performance Semitransparent Organic Solar Cells

Tao Xu, Baozhong Deng, Yanglin Zhao, Zihan Wang, Gaëtan Lévêque, Yannick Lambert, Bruno Grandidier, Shenghao Wang,* and Furong Zhu*


Semitransparent organic solar cells (ST-OSCs) can be made in different colors, allowing light to pass through, and yet absorb enough visible and near-infrared (NIR) light to generate electricity. However, it remains a challenge to achieve high performing ST-OSCs over the two competing indexes of power conversion efficiency (PCE) and average visible transmittance (AVT). This work reports an effort to develop record-performance ST-OSCs using a low/high index optical coupling layer (OCL) and a 2D photonic-structured antireflective (AR) coating. High-throughput optical screening is used to improve the understanding of OCL structure—performance relationships and the predicting of NIR absorption enhancement for ST-OSCs. The concurrent use of a low/high index Na_3AlF_6 (170 nm)/ZnS (110 nm) OCL, identified among about 200 thousand simulated device configurations and a 900 nm pitch-sized 2D photonic-structured AR coating, fabricated using nanoimprint lithography, enables the record-performance ternary PM6:BTP-eC9:L8-BO-based ST-OSCs, achieving simultaneously a record-high PCE of 15.2%, a high AVT of 32%, an impressive light utilization efficiency of 4.86%, and a favorable color-rendering index of 82. The results of the ST-OSCs demonstrated in this work provide an attractive option for a plethora of applications in self-powered greenhouses and building-integrated photovoltaic systems.

1. Introduction

Semitransparent solar cells have attracted increasing interest because of their potential applications in power-generating windows, building-integrated photovoltaic systems, and greenhouses.^[1–5] Compared to the inorganic semiconductor-based solar cells, organic solar cells (OSCs) can be made flexible, semitransparent and are light weight. The unique flexibility and semi-transparency feature also add a decorative and aesthetic dimension to the OSCs so that they can be used on curved and irregular surfaces – something that cannot be done using traditional rigid silicon solar cells.^[6] Therefore, development of high-performance semi-transparent organic solar cells (ST-OSCs) has attracted an increasing attention in the rapidly growing field of OSCs.^[7–10] Single junction OSCs with a power conversion efficiency (PCE) of over 19% have been demonstrated, due to the recent advances in nonfullerene acceptors (NFAs)

T. Xu, B. Deng, Y. Zhao
Sino-European School of Technology
Shanghai University
Shanghai 200444, China
Z. Wang, S. Wang
Materials Gerome Institute
Shanghai University
Shanghai 200444, China
E-mail: shenghaowang@shu.edu.cn

G. Lévêque, Y. Lambert, B. Grandidier
Univ. Lille
CNRS
Centrale Lille
Univ. Polytechnique Hauts-de-France
Junia-ISEN, UMR 8520 – IEMN, Lille 59000, France
F. Zhu
Department of Physics
Research Centre of Excellence for Organic Electronics and Institute
of Advanced Materials
Hong Kong Baptist University
Kowloon Tong, Hong Kong, China
E-mail: frzhu@hkbu.edu.hk

 The ORCID identification number(s) for the author(s) of this article can be found under <https://doi.org/10.1002/aenm.202301367>

© 2023 The Authors. Advanced Energy Materials published by Wiley-VCH GmbH. This is an open access article under the terms of the Creative Commons Attribution License, which permits use, distribution and reproduction in any medium, provided the original work is properly cited.

DOI: 10.1002/aenm.202301367

with excellent electron mobility, tunable energy levels and an extended absorption in the near-infrared (NIR) region. Advances in the NFA-based OSCs also offer an exciting opportunity for development of high-performance ST-OSCs through harnessing NIR portion of the sun light.^[11–16] Much progress has been made in improving the performance of the ST-OSCs,^[17–20] including the use of an aperiodic band-pass electrode for assisting in the NIR absorption.^[21] However, there is still a challenge achieving high-performance ST-OSCs over the two competing indexes of PCE and average visible transmittance (AVT) because of the trade-off between the absorption and transparency in the active layer.^[22]

Much effort has been devoted to enhancing the performance of ST-OSCs over the two competing indexes of PCE and AVT, such as incorporating newly developed low bandgap polymer donors with an enhanced absorption in the long wavelength region and using ternary blend systems having extended absorption in the NIR wavelength range.^[23–30] In addition to the advances in material innovation, a key technical development relies on the device design to improve the visible transparency while enhancing NIR absorption in the ST-OSCs.^[31–33] Optical engineering technologies employing photonic structures, such as optical coupling layer (OCL) and antireflective (AR) coating, have been applied to improve PCE and AVT of the ST-OSCs.^[34–38] The performance enhancement of the ST-OSCs incorporating two pairs of LiF/MoO₃-based photonic crystals was reported.^[39] The design of the OCL dielectric structures can be guided by simulation, leading for example to the selection of a low/high dielectric constant LiF/MoO₃ double layer OCL to achieve NIR absorption enhancement in the ST-OSCs.^[40] In addition to the improved absorption at long-wavelength, color-rendering index (CRI) is another important factor to consider for the performances of the ST-OSCs, which is related to the color neutrality, but no systematic analysis has been carried out so far.

In this work, a combination of low/high index double layer OCL and 2-D photonic-structured AR coating has been optimized to achieve NIR absorption enhancement, thereby improving the light utilization efficiency (LUE) and CRI in ST-OSCs. The device fabrication has been guided, at design and analysis level, using transfer matrix method (TMM) and finite element method (FEM) simulations to develop optimal combination of the low/high index double layer OCL and 2-D photonic-structured AR coating. By analyzing the photonic-structure–distinct optical phenomena relationships and predicting NIR absorption enhancement of ST-OSCs, high-throughput optical screening of ≈ 200 thousand different low/high index double layer OCLs, for example, the layer thickness, d_1 , and refractive index, n_1 , of the low index dielectric constant layer, and the layer thickness, d_2 , and refractive index, n_2 , of the high dielectric constant index layer in different double layer OCLs, has been systematically investigated. Our results reveal that the ST-OSCs with a Na₃AlF₆ (170 nm)/ZnS (110 nm)-based low/high index double layer OCL possess the best combination of a high PCE and a high AVT, prepared using a ternary blend system of a wide bandgap polymer donor, poly[[4,8-bis[5-(2-ethylhexyl)-4-fluoro-2-thienyl]benzo[1,2-b:4,5-b']dithiophene-2,6-diyl]-2,5-thiophenediyl[5,7-bis(2-ethylhexyl)-4,8-dioxo-4H,8H-benzo[1,2-c:4,5-c']dithiophene-1,3-diyl]-2,5-thiophenediyl] (PM6), and two narrow bandgap NFAs, 2,2'-[[12,13-bis(2-butylloctyl)-12,13-dihydro-3,9-dinonylbisthieno [2',3':4',5']

thieno[2',3':4',5']pyrrolo[3,2-e:2',3']-[2,1,3]benzothiadiazole-2,10-diyl]bis[methylidene]bis[propanedinitrile] (BTP-eC9) and 2,2'-((2Z,2'Z)-((3,9-bis(2-butylloctyl)-12,13-bis(2-ethylhexyl)12,13-dihydro-[1,2,5]thiadiazolo [3,4-e]thieno[2',3':4',5']thieno[2',3':4',5']pyrrolo-[3,2-g]thieno[2',3':4',5']thieno[3,2-b]indole-2, 10-diyl)bis(methanelylidene))bis(5,6-difluoro-3-oxo-2,3-dihydro-1H-indene-2,1-diylidene)) dimalononitrile (L8-BO). The weight ratio of PM6 to BTP-eC9 to L8-BO in the ternary bulk heterojunction (BHJ) and its layer thickness were optimized to enhance the LUE and CRI of the ST-OSCs. The use of a rear Na₃AlF₆ (170 nm)/ZnS (110 nm) double layer OCL and a front 2-D photonic-structured AR coating results in ternary PM6:BTP-eC9:L8-BO-based ST-OSCs having a record-high PCE of 15.2%, a high AVT of 32.0%, an impressive LUE of 4.86%, a favorable CRI of 82 and an improved aging stability.

2. Results and Discussion

Compared to the absorption profile of PM6 polymer donor, BTP-eC9 and L8-BO NFAs have a complementary absorption in the NIR wavelength region. A PCE of 18.46% was obtained for the PM6:BTP-eC9:L8-BO (1.0:0.4:0.8)-based opaque OSCs, as reported in our previous work.^[41] The weight ratio of PM6 to BTP-eC9 to L8-BO in the BHJ was further optimized for enhancing NIR absorption, thereby improving the performance of the ST-OSCs over the two competing indexes of PCE and AVT. The normalized absorption spectra measured for the pristine PM6, BTP-eC9 and L8-BO layers are shown in **Figure 1a**, and that measured for the ternary PM6:BTP-eC9:L8-BO blend layers, prepared using the precursor solutions with different weight ratios of PM6 to BTP-eC9 to L8-BO, are shown in **Figure 1b**. It shows that NIR light absorption of the ternary BHJ layers increases with the weight ratio of NFAs to polymer in the ternary blend layer. The surface morphology of the PM6:BTP-eC9:L8-BO blend layers with different weight ratios of PM6 to BTP-eC9 to L8-BO was analyzed using atomic force microscopy (AFM). A fiber-like feature structure in the blend film with a weight ratio of PM6 to BTP-eC9 to L8-BO of 1.0:0.4:0.8 can be clearly observed, as shown in **Figure S1**, Supporting Information.

The impact of the PM6 content on microstructure changes in the ternary blend films with different weight ratios of PM6 to BTP-eC9 to L8-BO of 1.0:0.4:0.8, 0.8:0.4:0.8, 0.6:0.4:0.8, and 0.4:0.4:0.8 and cell performance were also investigated. The increase in the domain size, as shown in AFM images in **Figure S1**, Supporting Information, is associated with the increase in aggregation of BTP-eC9 and L8-BO molecules due to the decrease in the PM6 in the blend layer. A fiber-like feature structure in the blend films with different weight ratios of PM6 to BTP-eC9 to L8-BO is observed. Similar microstructure features are also observed in the TEM images measured for the blend films with different weight ratios of PM6 to BTP-eC9 to L8-BO of 1.0:0.4:0.8 and 0.6:0.4:0.8, as shown in **Figure S2**, Supporting Information. TEM measurements agree with the AFM analysis in showing that PM6, BTP-eC9 and L8-BO have a good miscibility in these ternary blend layers, enhancing the performance of the optimized PM6:BTP-eC9:L8-BO-based ST-OSCs through enhanced absorption in the long wavelength range.

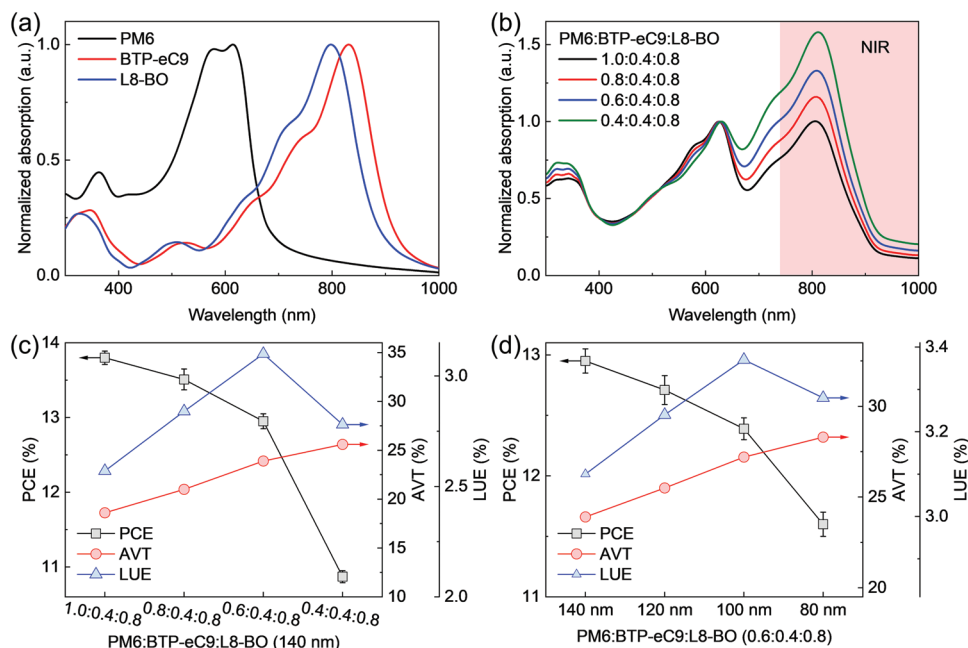


Figure 1. ST-OSCs without OCL. a) Normalized absorption spectra measured for the pristine PM6, BTP-eC9 and L8-BO films. b) Normalized absorption spectra measured for the PM6:BTP-eC9:L8-BO blend layers with different weight ratios of PM6 to BTP-eC9 to L8-BO. c) PCE, AVT, and LUE of the ST-OSCs with a 140 nm-thick BHJ, prepared using blend solutions having different weight ratios of PM6 to BTP-eC9 to L8-BO of 1.0:0.4:0.8, 0.8:0.4:0.8, 0.6:0.4:0.8, and 0.4:0.4:0.8. d) PCE, AVT and LUE measured for the PM6:BTP-eC9:L8-BO (0.6:0.4:0.8)-based ST-OSCs, prepared using the BHJ having different layer thicknesses of 140, 120, 100, and 80 nm.

2.1. ST-OSCs without OCL

A set of ST-OSCs, comprising a layer configuration of indium tin oxide (ITO)/poly(3,4-ethylenedioxythiophene):poly(styrenesulfonate) (PEDOT:PSS)/BHJ/ $C_{26}H_{20}N_{22}$,9-dimethyl-4,7-diphenyl-1,10-phenanthroline (BCP)/Au/Ag, prepared using BHJ with different weight ratios of PM6 to BTP-eC9 to L8-BO was fabricated. A 40 nm-thick PEDOT:PSS hole transporting layer (HTL), a 140 nm-thick PM6:BTP-eC9:L8-BO-based active layer, an 8.0 nm-thick BCP electron transporting layer (ETL), and a bilayer Au (1 nm)/Ag (10 nm) upper semitransparent electrode were used to improve the charge collection in the cells. The addition of an ultrathin Au interlayer improves the wettability of the upper Ag contact favoring formation of a uniform transparent upper Au (1.0 nm)/Ag (10 nm) electrode.^[40,42–45] The current density–voltage (J – V) characteristics, the external quantum efficiency (EQE), and the visible light transparency spectra of the ST-OSCs, prepared using BHJ layer with different weight ratios PM6 to BTP-eC9 to L8-BO of 1.0:0.4:0.8, 0.8:0.4:0.8, 0.6:0.4:0.8, and 0.4:0.4:0.8, are shown in Figure S3a,b, Supporting Information. EQE spectra measured for ST-OSCs with different weight ratios of PM6 to BTP-eC9 to L8-BO of 1.0:0.4:0.8, 0.8:0.4:0.8, 0.6:0.4:0.8, and 0.4:0.4:0.8 suggest that further reducing the concentration of PM6 in the blend layer, for example, 0.4:0.4:0.8, deviates the optimal exciton dissociation, thereby resulting in a decrease in generation of photoelectrons, hence a reduction in EQE, as shown in Figure S3, Supporting Information. A summary of the short circuit current density (J_{SC}), open circuit voltage (V_{OC}), fill factor (FF) and PCE is listed in Table S1, Supporting Information. AVT of the ST-OSCs can be calculated according to the

following equation:

$$AVT = \frac{\int_{370}^{740} T(\lambda) V(\lambda) F(\lambda) d\lambda}{\int_{370}^{740} V(\lambda) F(\lambda) d\lambda} \quad (1)$$

where $T(\lambda)$ is the transparency spectrum of the ST-OSCs, $V(\lambda)$ is the spectral luminous-efficiency function of the human eye, and $F(\lambda)$ is the flux of the AM1.5G irradiation.

PCE, AVT, and LUE measured for the ST-OSCs with a 140 nm-thick BHJ having different weight ratios of PM6 to BTP-eC9 to L8-BO of 1.0:0.4:0.8, 0.8:0.4:0.8, 0.6:0.4:0.8, and 0.4:0.4:0.8 are shown in Figure 1c. A PCE of 13.80% is obtained for the ST-OSC with a PM6:BTP-eC9:L8-BO (1.0:0.4:0.8)-based BHJ layer as compared to that of the ST-OSC with a PM6:BTP-eC9:L8-BO (0.4:0.4:0.8)-based BHJ layer (10.87%), whereas an AVT of 25.6% is achieved for the PM6:BTP-eC9:L8-BO (0.4:0.4:0.8)-based ST-OSCs as compared to that of the PM6:BTP-eC9:L8-BO (1.0:0.4:0.8)-based ST-OSCs, due to the trade-off between PCE and AVT. LUE, an important figure of merit, was used to assess the performance of the ST-OSCs, which is defined by:

$$LUE = PCE \times AVT \quad (2)$$

A LUE of 3.10%, a PCE of 12.95%, and an AVT of 23.9% were obtained for the ST-OSCs with a 140 nm-thick PM6:BTP-eC9:L8-BO (0.6:0.4:0.8)-based BHJ layer. In addition to LUE, PCE and AVT, the color neutrality of ST-OSCs is another important factor

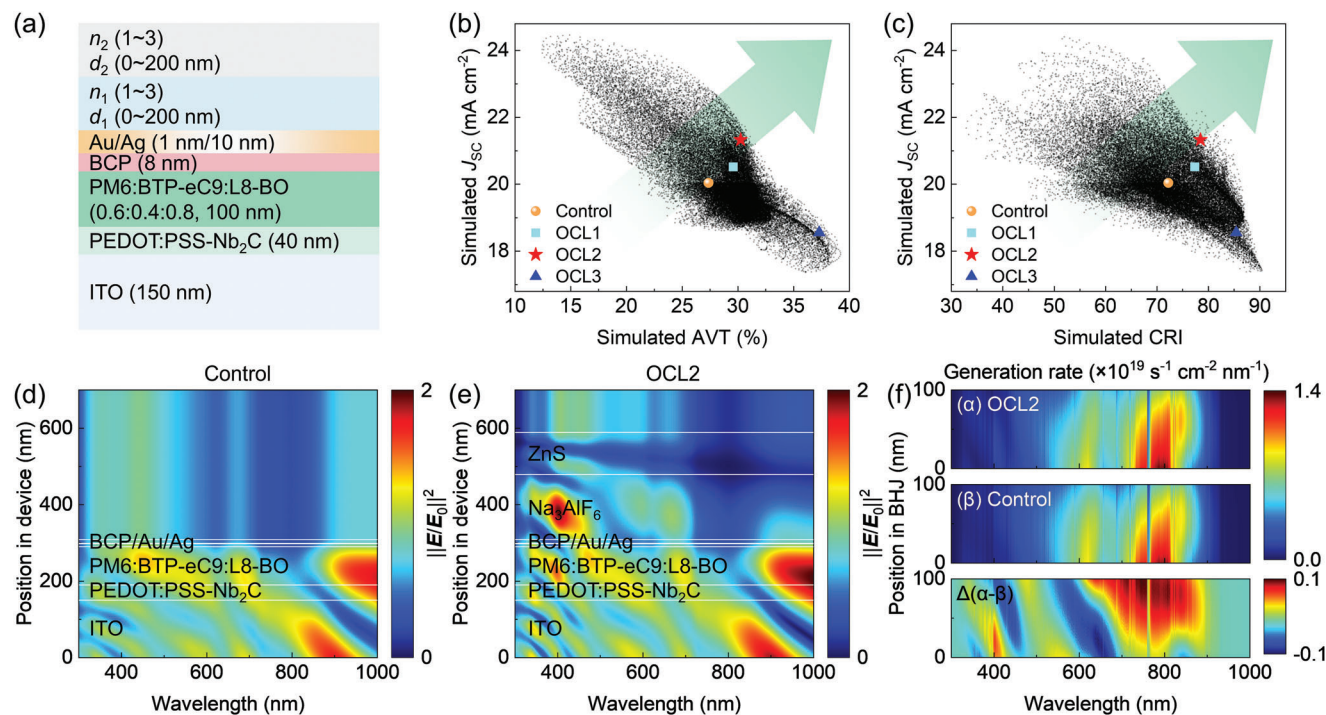


Figure 2. ST-OSCs with an OCL. a) Cross-sectional view of a ST-OSC with a low/high dielectric constant double layer OCL. Contour map of b) J_{sc} -AVT and c) J_{sc} -CRI as the functions of the refractive index and layer thickness of the double layer OCL, calculated for n_1 and n_2 over the refractive index range from 1.0 to 3.0, and d_1 and d_2 over the thickness range from 0 to 200 nm. The data points, for example, the circle, square, star and triangle symbols, in the contour map are the J_{sc} and AVT values calculated for the control cell without OCL, and the ST-OSCs with different OCLs of LiF (150 nm)/MoO₃ (100 nm) (OCL1), Na₃AlF₆ (170 nm)/ZnS (110 nm) (OCL2), and ZnS (30 nm) (OCL3). The green arrow indicates the possible materials choices in the double layer OCL for realizing simultaneously a high J_{sc} and a high AVT in the ST-OSCs. Profiles of the electric field distribution calculated for d) the control ST-OSC without OCL, and e) the one with an OCL2. (f) Profiles of the exciton generation in the active layers of the control device and the ST-OSCs with an OCL2, and the difference in the exciton generation rate between the control and the ST-OSCs with an OCL2.

in practical application, which can be presented using (x, y) coordinates in the Commission Internationale de l'Éclairage (CIE) chromaticity diagram.^[46] The corresponding CIE (x, y) coordinates of the ST-OSCs, having BHJ prepared using different weight ratios of PM6 to BTP-eC9 to L8-BO, are shown in Figure S3c, Supporting Information. It shows that the CIE (x, y) coordinates of the ST-OSCs having a lower PM6 content in the BHJ moves to the “cool white” side on the Planckian locus in the chromaticity diagram.

The performance of the ST-OSCs over the two competing indexes of PCE and AVT can be further optimized by adjusting the thickness of the active layer. A set of ST-OSCs with different BHJ thicknesses of 140, 120, 100 and 80 nm, having an optimal weight ratio of PM6 to BTP-eC9 to L8-BO of 0.6:0.4:0.8, was fabricated. PCE, AVT and LUE measured for the PM6:BTP-eC9:L8-BO (0.6:0.4:0.8)-based ST-OSCs having different BHJ thicknesses are shown in Figure 1d. J - V characteristics, EQE spectra, transmission spectra and CIE (x, y) coordinates obtained for the set of the ST-OSCs are shown in Figure S4, Supporting Information. A summary of device performances measured for the ST-OSCs without OCL is listed in Table S2, Supporting Information, revealing PM6:BTP-eC9:L8-BO (0.6:0.4:0.8)-based ST-OSCs with a 100 nm-thick BHJ have a PCE of 12.39%, an AVT of 27.2%, and an optimized LUE of 3.37%. In addition to optimizing the active layer, a PEDOT:PSS-Nb₂C hybrid HTL was used to enhance the PCE of the ST-OSCs without sacrificing the AVT, as reported in

our previous work.^[41] A summary of device performances measured for the ST-OSCs with the hybrid HTL is listed in Table S3, Supporting Information, giving an improved PCE of 13.25%, a similar AVT of 27.2%, and a higher LUE of 3.60%, as compared to that of the device with a pristine PEDOT:PSS HTL. In this work, the performance of a control ST-OSC with a 100 nm-thick PM6:BTP-eC9:L8-BO (0.6:0.4:0.8)-based BHJ and a PEDOT:PSS-Nb₂C hybrid HTL was used for comparison study.

2.2. ST-OSCs with a Low/High Index OCL

The performance of the ST-OSCs, comprising a layer configuration of glass/ITO/PEDOT:PSS-Nb₂C (40 nm)/PM6:BTP-eC9:L8-BO (0.6:0.4:0.8) (100 nm)/Au(1.0 nm)/Ag(10 nm)/bilayer low/high index OCL, was further analyzed over the two competing indexes of PCE and AVT. The possible layer configurations of the ST-OSCs with a low/high index OCL have been examined using high-throughput optical screening for improving the visible light transparency and NIR absorption enhancement. This was realized by computing different combinations of the bilayer low/high index OCLs, for example, d_1 and n_1 of the low index layer, and d_2 and n_2 of the high index layer in the double layer OCLs. The cross-sectional view of the ST-OSC with a low/high dielectric constant double layer OCL is shown in Figure 2a. The measured wavelength-dependent refractive index and extinction

coefficient of the functional layers used in the TMM and FEM simulations are shown in Figure S5, Supporting Information. The optical profile in the ST-OSCs with a low/high index double layer OCL was analyzed and optimized, taking the advantage of tailored absorption of the ternary PM6:BTP-eC9:L8-BO (0.6:0.4:0.8) blend layer for NIR absorption enhancement and improved visible light transparency, predicting the J_{SC} and AVT in the ST-OSCs. High-throughput optical screening for predicting the possible material combinations in the bilayer low/high index OCL was analyzed. For such a purpose, refractive indices n_1 and n_2 were varied over the index range from 1.0 to 3.0 with an interval of 0.1, and the corresponding layer thicknesses d_1 and d_2 in the low/high index double layer OCL were varied over the thickness range from 0 to 200 nm independently, with an interval of 10 nm. A total of ≈ 200 thousand device configurations were simulated through permutations of low/high index layers with different values of n_1 , n_2 , d_1 , and d_2 for realizing simultaneous high visible light transparency and NIR absorption enhancement, and thereby leading to a combination of high PCE and AVT.

A contour map of J_{SC} and AVT as function of the refractive index and layer thickness of the low/high dielectric index double layer OCL is shown in Figure 2b. Although there is a trade-off between visible light transparency and J_{SC} in ST-OSCs, the high-throughput optical screening reveals that the performance of the ST-OSCs can be optimized over the two competing indexes of PCE and AVT by incorporating an appropriate low/high dielectric constant double layer OCL. This is indicated by the green arrow which points to the best materials choice and thickness optimization in the double layer OCL for realizing simultaneously a high J_{SC} and a high AVT in the ST-OSCs. The data points in the contour map, for example, the yellow circle, cyan square, red star and blue triangle symbols, are the J_{SC} and AVT values calculated for the control cell without OCL, and the ST-OSCs with different OCLs of LiF (150 nm)/MoO₃ (100 nm) (OCL1), Na₃AlF₆ (170 nm)/ZnS (110 nm) (OCL2), and ZnS (30 nm) (OCL3). The refractive index of the dielectric materials, for example, Na₃AlF₆/ZnS, are less dependent on the wavelength over the wavelength range of interest studied in this work, for example, over the wavelength range from 400 to 1000 nm, shown Figure S5, Supporting Information. Therefore, it is a reasonable approximation to consider wavelength-independent refractive index for in the high-throughput optical screening. Selection of the suitable dielectric OCL materials with desired combination of n and d can then be guided for achieving high performance ST-OSCs according to the simulation results, for example, the data points in Figure 2b. In this work, an optimal bilayer OCL configuration of Na₃AlF₆ ($n_1 = 1.3$, $d_1 = 170$ nm)/ZnS ($n_2 = 2.4$, $d_2 = 110$ nm)-based low/high index double layer OCL is obtained for high performance ST-OSCs.

Additional insights for the J_{SC} –AVT relationships and the prediction of the ST-OSCs performance with different OCLs are shown in Figure S6, Supporting Information. The use of a single layer OCL, for example, ZnS ($n = 2.4$, $d = 30$ nm) labeled as OCL3 (triangle) in Figure 2b, would generally assist in improving AVT at a cost of J_{SC} , as reported in our recent work.^[47] A summary of the J_{SC} –AVT relationships for the ST-OSCs having different combinations of realistic OCLs is listed in Table S4, Supporting Information. Among the existing OCLs, an optimal OCL of Na₃AlF₆ ($n_1 = 1.3$, $d_1 = 170$ nm)/ZnS ($n_2 = 2.4$, $d_2 = 110$ nm), labeled as

OCL2 (red star) in Figure 2b, was identified, leading to the evident improvements in both J_{SC} and AVT as compared to that of the ST-OSCs with an OCL1 (cyan square).

In addition to identifying the optimal low/high index bilayer OCL configuration and predicting the performance of the ST-OSCs over the two competing indexes of PCE and AVT, the color neutrality of ST-OSCs was also analyzed. CIE (x , y) coordinates of the ST-OSCs closer to the Planckian locus in the chromaticity diagram represent the better color neutrality, which can be quantified by CRI over the scale from 0 to 100. J_{SC} –CRI relationships calculated for different ST-OSCs are shown in Figure 2c. It shows clearly that the ST-OSC with an OCL2 has a superior J_{SC} and a higher CRI as compared to that of the ST-OSCs with an OCL1 and the control ST-OSCs without OCL, revealing the impact of using an optimal low/high index double layer OCL, for example, Na₃AlF₆ (170 nm)/ZnS (110 nm), on the color appearance of the ST-OSCs.

The profiles of the optical field $|E(x, \lambda)|^2$ distribution calculated for the control ST-OSC without OCL and the ST-OSC with an optimal OCL of Na₃AlF₆ (170 nm)/ZnS (110 nm) (OCL2) are shown in Figure 2d,e. It reveals that the use of an appropriate OCL, for example, an OCL2, in the ST-OSC favors the light absorption enhancement, particularly over the long wavelength range. This can be further manifested by analysing the profiles of the exciton generation in the active layer of a ST-OSC with an OCL2 and that in a control ST-OSC without OCL, as shown in Figure 2f. It becomes clear that the use of the optimal low/high index double layer OCL assists in enhancing both visible light transparency and absorption over the long wavelengths of >700 nm, achieving the high-performing ST-OSCs over the two competing indexes of PCE and AVT. Figure S7, Supporting Information shows the optical field distribution of the ST-OSCs with a single layer OCL3 for comparison. It reveals that increase in transparency of the ST-OSCs with a single OCL also induces a decrease in absorption of active layer over the NIR wavelength range. Therefore, increase in AVT of the ST-OSCs with a single OCL does not help NIR absorption enhancement, and thereby leading to a decrease in J_{SC} . In this work, the absorption in the active layer in ST-OSCs has been optimized using the optimal combination of bilayer OCL.

The fabrication of the ST-OSCs has been guided, at design and analysis level, using high-throughput optical screening to predict the optimal combination of the low/high index double layer OCL. J – V characteristics, transmission spectra, and chromaticity coordinates obtained for a control device without OCL and the ST-OSCs with different OCLs of OCL1, OCL2, or OCL3 are shown in Figure S8, Supporting Information) Table S5, Supporting Information summarizes the performance of different ST-OSCs. The experimental results reveal clearly that the use of a low/high index Na₃AlF₆ (170 nm)/ZnS (110 nm) OCL enables a simultaneous improvement in PCE and AVT as compared to that of the ST-OSC with a LiF (150 nm)/MoO₃ (100 nm) OCL, leading to a combination of a higher PCE of 14.42%, an AVT of 30.2%, and a LUE of 4.35%. It is clear that simulation supports the experimental results. A CRI of 81.7 is also observed for the ST-OSC with an OCL2, which is more preferred as compared to that of a control ST-OSC without OCL (CRI = 73.4). For comparison, the experimental results indicate that the ST-OSCs with a single layer OCL, for example, ZnS (30 nm), have generally a higher LUE (4.50%) and a relatively higher AVT (36.5%), however, at a

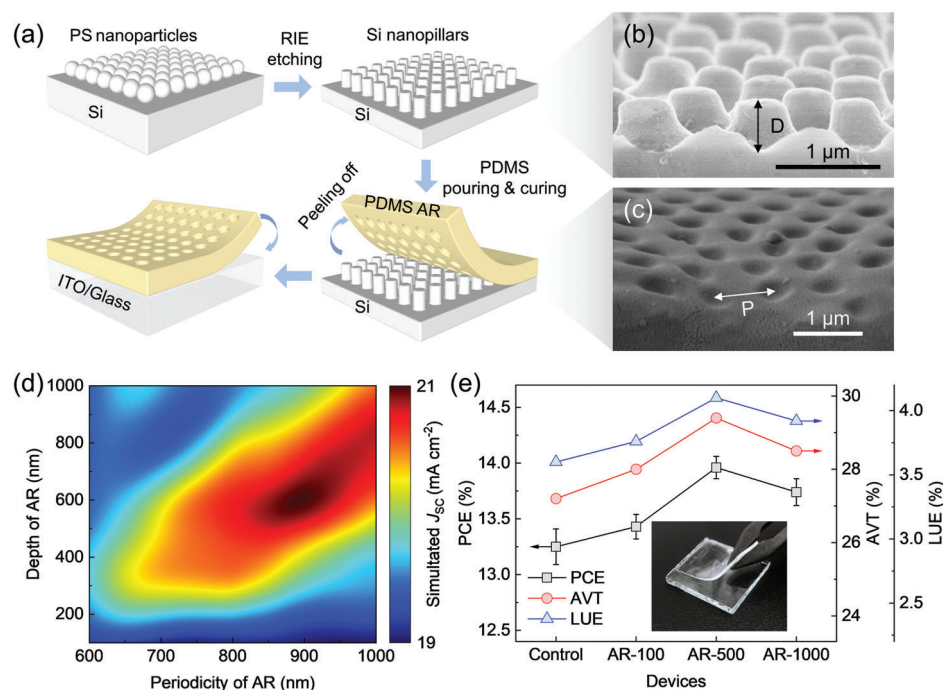


Figure 3. ST-OSCs with an AR coating. a) Schematic diagram illustrating the fabrication process of the photonic-structured AR coating prepared using nanoimprint lithography. SEM images measured for the surfaces of photonic-structured b) Si mould and c) PDMS AR coating. d) Contour map of the theoretical prediction of J_{SC} as functions of the depth and periodicity of photonic-structures in the AR coatings used in the ST-OSCs. e) PCE, AVT and LUE obtained for the control device and the ST-OSCs with the 900 nm pitch-sized PDMS AR coatings having different nanohole depths of 100, 500, and 1000 nm, for example, AR-100, AR-500, and AR-1000. Inset in Figure 3e: photograph taken for the photonic-structured PDMS AR coating on the glass substrate.

cost of reduction in PCE (12.34%). Our results suggest that use of a single layer OCL has a limitation for improving the performance of the ST-OSCs over the two competing indexes of PCE and AVT simultaneously. To conclude this part, the experimental results agree well with theoretical prediction in showing that the use of an optimal low/high index double layer OCL favors the performance enhancement of the ST-OSCs over the two competing indexes of PCE and AVT.

2.3. ST-OSCs with a 2-D Photonic-Structured AR Coating

We also examined the increase in LUE of the ST-OSCs by incorporating a 2-D photonic-structured AR coating to mitigate the ambient reflection at the air/glass interface. A schematic diagram illustrating the fabrication process of the photonic-structured AR coating, prepared using nanoimprint lithography, is shown in Figure 3a. The photonic-structured Si mould, with a pitch size of 900 nm, optimized by the FEM simulation, was fabricated using the nanosphere lithography. The height and periodicity of the nanopillars in the Si mould are optimized for realizing the minimal ambient reflection by the ST-OSCs. The fabrication process of the photonic-structured Si mould is described in our previous works^[48–50] and illustrated in Figure S9, Supporting Information. An inverted polydimethylsiloxane (PDMS) photonic-structured AR coating formed on the Si mould was carefully peeled-off and attached on the glass side of the ST-OSCs. Scanning electron microscopy (SEM) images measured for the photonic-structured Si

mould and the PDMS AR coating are shown in Figure 3b,c. The PDMS AR coatings with an inverted photonic structure of the Si mould are clearly seen.

The contour map of the J_{SC} calculated for the ST-OSCs, comprising a layer configuration of AR coating/glass/ITO/PEDOT:PSS-Nb₂C (40 nm)/PM6:BTP-eC9:L8-BO (0.6:0.4:0.8) (100 nm)/Au(1.0 nm)/Ag(10 nm), as functions of the depth and periodicity of the 2-D photonic-structures is shown in Figure 3d. The FEM simulation reveals that a maximum enhancement in J_{SC} can be obtained in the ST-OSCs with a 2-D photonic-structured AR coating having a pitch size of 900 nm and nanohole depth over the range from 500 to 600 nm. 2-D photonic-structured AR coatings with a pitch size of 900 nm and three different nanohole depths of 100, 500, and 1000 nm were fabricated, for example, denoted as AR-100, AR-500, and AR-1000, respectively. The transmission spectra measured for the bare ITO/glass and the ones with the 2-D photonic-structured AR coatings having different nanohole depths are shown in Figure S10, Supporting Information. The bare glass/ITO substrate has an average visible light transparency of 85.7%, which is obviously lower than that measured for the AR-100/glass/ITO (88.9%), AR-500/glass/ITO (90.5%), and AR-1000/glass/ITO (87.9%), revealing the effect of incorporating a 2-D photonic-structured AR coating on improvement in the visible light transparency of the ST-OSCs. A set of ST-OSCs with different AR coatings was subsequently fabricated. PCE, AVT, and LUE obtained for the control device and ST-OSCs with a 900 nm pitch-sized PDMS AR coatings having different nanohole depths of 100, 500, and 1000 nm

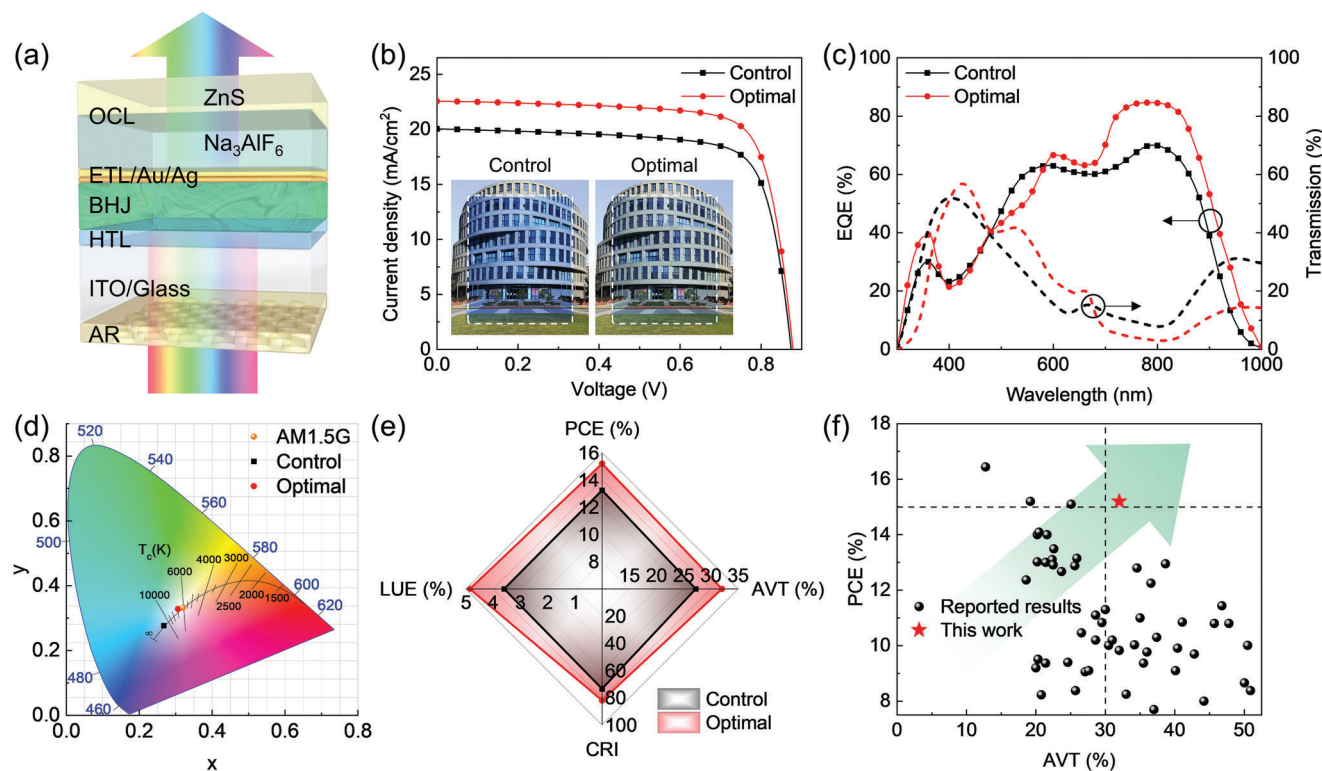


Figure 4. ST-OSCs with a low/high index OCL and a 2-D photonic-structured AR coating. a) Cross-sectional view of the ST-OSC with a front photonic-structured AR coating and a rear low/high dielectric constant double layer OCL. b) J - V characteristics, inset in (b): Photographs taken for a control cell and an optimized ST-OSC with a photonic-structured AR coating and a bilayer OCL. c) EQE and transmission spectra, and d) CIE (x , y) coordinates obtained for the control device and the ST-OSC with a front photonic-structured AR coating and a rear low/high dielectric constant double layer OCL. e) A comparison of device performance, including PCE, AVT, LUE and CRI, obtained for the control ST-OSC and the ST-OSCs having a low/high index double layer OCL and a photonic-structured AR coating. f) Comparison of the PCE and AVT of the ST-OSCs demonstrated in this work and the ones reported recently by different groups is listed in Table S7, Supporting Information.

are shown in Figure 3e. Photograph taken for a 2-D photonic-structured AR layer coated glass/ITO substrate is shown in the inset of Figure 3e. The corresponding J - V characteristics and transmission spectra measured for the ST-OSCs with different 2-D photonic-structured PDMS AR coatings of AR-100, AR-500, and AR-1000 are shown in Figure S11, Supporting Information. A summary of the photovoltaic parameters measured for the control device and the ST-OSCs with different AR coatings is listed in Table S6, Supporting Information. It shows that the ST-OSCs with a 2-D photonic-structured AR-500 coating have a relatively higher PCE of 13.96% and an AVT of 29.4%, yielding an LUE of 4.10% that is 14% higher than that of the control device without AR coating (LUE = 3.60%). Again, the experimental results support the theoretical simulation in showing that use of a 2-D photonic-structured AR coating assists in improving the PCE and AVT of the ST-OSCs, realized due to the light trapping and anti-reflection enabled by the 2-D photonic-structured AR coating.

2.4. ST-OSCs with a Low/High Index OCL and a 2-D Photonic-Structured AR Coating

Taking the advantage of the optical coupling effect and the anti-reflection feature of the photonic-structured AR coating, high-

performance PM6:BTP-eC9:L8-BO (0.6:0.4:0.8)-based ST-OSCs with a front photonic-structured AR coating, for example, AR-500, and a rear low/high dielectric constant double layer OCL, for example, Na_3AlF_6 (170 nm)/ ZnS (110 nm), can then be finally realized. The cross-sectional view of the ST-OSC with a front photonic-structured AR coating and a rear low/high index double layer OCL is shown in Figure 4a. J - V characteristics measured for the control ST-OSC without OCL and the ST-OSCs with an optimal OCL and a 2-D photonic-structured AR coating are shown in Figure 4b. Photographs taken for the control device and the ST-OSC with an OCL and a 2-D photonic-structured AR coating are shown in the inset of Figure 4b, showing good visible light transparency and color neutrality. Table 1 lists the corresponding photovoltaic parameters measured for the control device, the ST-OSCs with an optimal OCL, the ST-OSCs with an optimal 2-D photonic-structured AR coating, and ones having both an optimal front AR coating and an optimal rear OCL. It shows that the ST-OSCs, having an optimal rear OCL and an optimal front 2-D photonic-structured AR coating, possess simultaneously a record-high PCE of 15.2% and a high AVT of 32.0%, outperforming the PCE (13.25%) and AVT (27.2%) of the control ST-OSC without OCL and 2-D photonic-structured AR coating.

The improvement in the optimal ST-OSCs over the two competing indexes of PCE and AVT is due to the NIR absorption

Table 1. Summary of photovoltaic parameters measured for the 100 nm-thick PM6:BTP-eC9:L8-BO (0.6:0.4:0.8)-based control ST-OSC with a PEDOT:PSS-Nb₂C hybrid HTL, the ST-OSCs with an OCL, the ST-OSCs with a photonic-structured AR coating and the ST-OSCs with a front photonic-structured AR coating and a rear double layer OCL. The results were averaged from the measurements of 10 cells.

	J_{SC} [mA cm ⁻²]	J_{cal} [mA cm ⁻²] ^{a)}	V_{OC} [V]	FF [%]	PCE [%]	AVT [%]	LUE [%]	CRI
Control	20.02 ± 0.26	19.40	0.87 ± 0.01	75.80 ± 0.17	13.25±0.17	27.2	3.60	73.4
With an OCL2	21.34 ± 0.28	20.87	0.88 ± 0.01	76.98 ± 0.50	14.42±0.19	30.2	4.35	81.7
With an AR-500 coating	21.14 ± 0.12	20.71	0.87 ± 0.01	75.54 ± 0.12	13.96±0.11	29.4	4.10	73.6
Optimized ST-OSCs ^{b)}	22.55 ± 0.28	21.94	0.88 ± 0.01	76.79 ± 0.33	15.20±0.15	32.0	4.86	82.0

^{a)} J_{SC} calculated from EQE spectra; ^{b)} The optimized ST-OSCs with a combination of a low/high dielectric constant Na₃AlF₆ (170 nm)/ZnS (110 nm) double layer OCL and a photonic-structured AR-500 coating.

enhancement, demonstrated by the EQE, as shown in Figure 4c. A remarkable increase in EQE of the optimal ST-OSCs over the long wavelength range from 700 to 1000 nm, together with a simultaneous improvement in transmission over the visible light wavelength range, is realized. The use of an optimal OCL2 and an optimal 2-D AR-500 coating leads to an outstanding LUE of 4.86%, which is evidently higher than that of the control device (LUE = 3.60%). The quantum utilization efficiency (QUE), an overall figure of merit of ST-OSCs, was also used to evaluate the light utilization efficiency in the ST-OSCs with different layer configurations. QUE is defined by:

$$QUE(\lambda) = EQE(\lambda) + T(\lambda) \quad (3)$$

where $T(\lambda)$ is the transmission spectra of the ST-OSCs. QUE spectra obtained for a control device and the ST-OSCs with an optimal OCL and an optimal 2-D photonic-structured AR coating are shown in Figure S12, Supporting Information. The transmission measured for a glass/ITO substrate is also presented for comparison study. It becomes clear that the ST-OSCs with an optimal OCL and a 2-D photonic-structured AR-500 coating have a broadband enhancement in QUE, achieving a maximum QUE of 91%, as compared to that of a control device (QUE = 86%).

CIE (x, y) coordinates of different ST-OSCs were calculated, the results are shown in Figure 4d. It shows that the ST-OSCs with an OCL2 and an AR-500 coating have CIE (x, y) coordinates of (0.306, 0.328), which are nearer to the equal energy white of the spectrum on Planckian locus as compared to the “cool white” of the spectrum seen for the control device (0.267, 0.277). A CRI of 82 is obtained for the ST-OSCs with an OCL2 and an AR-500 coating, which is obviously higher than that of the control device (CRI = 73.4), revealing the improved color neutrality. The advantages of incorporating an optimal bilayer low/high index OCL and a 2-D photonic-structured AR coating for high-performing ST-OSCs are clearly revealed in the spider diagram, as shown in Figure 4e, revealing the superior performance of the optimized ST-OSCs in PCE, AVT, LUE, and CRI to that of the control ST-OSC. The performance of the ST-OSCs demonstrated in this work are very encouraging, achieving simultaneously a record-high PCE of 15.20% and a high AVT of 32.0%, outperforming that of the ST-OSCs with an AVT of >30% reported recently by different groups, as shown in Figure 4f.

Finally, the effect of the bilayer low/high index OCL on the stability of the ST-OSCs was carried out using an aging test through monitoring the performance of different ST-OSCs. The devices were unencapsulated and stored in a N₂-purged glove box with

O₂ and H₂O levels <0.1 ppm, at room temperature. In addition to the desired optical effect, the use of OCL also serves as a barrier layer, preventing encroachment of moisture and oxygen into the active layer, which is beneficial for ensuring the long-term stability of the ST-OSCs. The normalized PCE of the control device and the optimal ST-OSC as a function of the aging time is shown in Figure S13, Supporting Information. It shows that the ST-OSCs with an OCL2 maintains 90% of the initial PCE after 700 h of the aging test, which is much higher than that of the control device without OCL (79%). The results of this work demonstrate the technology advances in ST-OSCs over the two-competing index of PCE and AVT as well as the benefits of using a low/high dielectric constant double layer OCL and a 2-D photonic-structured AR coating for achieving record-performance and stable ST-OSCs.

3. Conclusion

In summary, the performance of the ST-OSCs has been optimized over the two competing indexes of PCE and AVT through NIR absorption enhancement. High-throughput optical screening provides improved understanding of the PCE–AVT relationships and allows to identify the optimal combination of a 2-D photonic-structured AR coating and a bilayer low/high index OCL for high-performance ST-OSCs. PM6:BTP-eC9:L8-BO-based ST-OSCs, with a low/high index Na₃AlF₆ (170 nm)/ZnS (110 nm) OCL and an optimized 900 nm pitch-sized photonic-structured AR coating, possess simultaneously a record-high PCE of 15.2%, a high AVT of 32.0%, an impressive high LUE of 4.86%, and a favorable high CRI of 82. The outcomes of the high performing ST-OSCs developed in this work emphasizes on the key role of material/geometry screening to identify the best configuration of future ST-OSCs suitable for various applications in power generating windows, mobile electronics, smart sensors, automotive, and green-houses.

4. Experimental Section

Theoretical Simulation: The wavelength-dependent transmission, $T(\lambda)$, absorption, $A(\lambda)$, and the profile of the electric field, $E(x, \lambda)$, in the ST-OSCs were analyzed using TMM simulation over the wavelength range from 300 to 1000 nm. Refractive indices of ITO, Au and Ag layers are taken from refractiveindex.info database. The optical constants of the functional layers of the PM6:BTP-eC9:L8-BO (0.6:0.4:0.8) blend layer, PEDOT:PSS-Nb₂C, Na₃AlF₆ and ZnS were measured using variable angle

spectroscopic ellipsometry (VASE). In the simulation, considering incoming light from the glass side and normal to the cell, and the functional layers are regarded as the homogenous media with the optical properties determined by the wavelength dependent optical constants. Assuming no non-geminate recombination losses, the theoretical prediction of the maximum J_{SC} in the ST-OSCs was calculated using the following expressions:

$$EQE(\lambda) = \int \frac{2\pi\epsilon_0cn(\lambda)k(\lambda)}{\lambda} |E(x, \lambda)|^2 dx \quad (4)$$

$$J_{SC} = \int \frac{EQE(\lambda)F(\lambda)\lambda e}{hc} d\lambda \quad (5)$$

where ϵ_0 is vacuum permittivity, c is the speed of light, $n(\lambda)$ and $k(\lambda)$ are the wavelength dependent refractive index and extinction coefficient of the active layer, x is position of the electric field in the active layer, e is the elementary charge and h is Planck constant.

CRI was calculated using the following equations:

$$CRI = \frac{1}{8} \sum_{i=1}^8 (100 - 4.6\Delta E_i) \quad (6)$$

$$\Delta E_i = \sqrt{(L_i^* - L_{test}^*)^2 + (a_i^* - a_{test}^*)^2 + (b_i^* - b_{test}^*)^2} \quad (7)$$

where ΔE is chromatic aberration, L^* , a^* , and b^* are the chromatic coordinates in CIE 1976 Lab color space and are defined as follows:

$$\begin{cases} L^* = 116f\left(\frac{Y}{Y_0}\right) - 16 \\ a^* = 500\left[f\left(\frac{X}{X_0}\right) - f\left(\frac{Y}{Y_0}\right)\right] \\ b^* = 200\left[f\left(\frac{Y}{Y_0}\right) - f\left(\frac{Z}{Z_0}\right)\right] \end{cases} \quad (8)$$

$$f(x) = \begin{cases} \sqrt[3]{x}, & x > \left(\frac{6}{29}\right)^3 \\ \frac{841}{108}x + \frac{4}{29}, & x \leq \left(\frac{6}{29}\right)^3 \end{cases} \quad (9)$$

where X , Y , Z are the tristimulus values which can be calculated as follows:

$$\begin{cases} X_i = \int_{380}^{780} F(\lambda) S_i(\lambda) R(\lambda) d\lambda \\ Y_i = \int_{380}^{780} F(\lambda) S_i(\lambda) G(\lambda) d\lambda \\ Z_i = \int_{380}^{780} F(\lambda) S_i(\lambda) B(\lambda) d\lambda \end{cases} \quad (10)$$

$$\begin{cases} X_{test} = \int_{380}^{780} F(\lambda) T(\lambda) S_i(\lambda) R(\lambda) d\lambda \\ Y_{test} = \int_{380}^{780} F(\lambda) T(\lambda) S_i(\lambda) G(\lambda) d\lambda \\ Z_{test} = \int_{380}^{780} F(\lambda) T(\lambda) S_i(\lambda) B(\lambda) d\lambda \end{cases} \quad (11)$$

where $S_i(\lambda)$ are the spectra of 8 standard color samples used in the CRI calculation, $R(\lambda)$, $G(\lambda)$, $B(\lambda)$ are the tristimulus functions specified by CIE. X_0 , Y_0 , Z_0 are those of AM1.5G and are calculated by removing $S_i(\lambda)$ part. (L_i^*, a_i^*, b_i^*) and $(L_{test}^*, a_{test}^*, b_{test}^*)$ are calculated using (X_i, Y_i, Z_i) and $(X_{test}, Y_{test}, Z_{test})$, respectively.

Exciton generation rate, $G(x, \lambda)$, in the ST-OSCs was calculated using the following equation:

$$G(x, \lambda) = \frac{2\pi\epsilon_0nkF(\lambda)}{h} |E(x, \lambda)|^2 \quad (12)$$

The algorithms were written in Python. The devices comprise a layer configuration of ITO (150 nm)/PEDOT:PSS-Nb₂C (40 nm)/PM6:BTP-eC9:L8-BO (0.6:0.4:0.8) (100 nm)/BCP (8.0 nm)/Au (1.0 nm)/Ag (10 nm)/low index layer ($n_1 = \approx 1-3$, $d_1 = \approx 0-200$ nm)/high index layer ($n_2 = \approx 1-3$, $d_2 = \approx 0-200$ nm), with n_1 , n_2 , d_1 , d_2 varied independently. The step of variation is 0.1 for n and 10 nm for d . In total, the performance of 19 4481 ST-OSCs with different OCL combinations of n_1 , n_2 , d_1 , d_2 was analyzed for J_{SC} , AVT and CRI.

The performance of the ST-OSCs with a 2-D photonic-structured AR coating was analyzed using the COMSOL Multiphysics. The periodicity of 2-D photonic structured is defined by the dimension of the simulation unit. The photonic-structured AR coatings, with a pitch size range from 600 to 1000 nm and a nanohole depth range from 100 to 1000 nm, were examined for the performance of the ST-OSCs with a layer configuration of AR coating/glass/ITO (150 nm)/PEDOT:PSS-Nb₂C (40 nm)/PM6:BTP-eC9:L8-BO (0.6:0.4:0.8) (100 nm)/BCP (8.0 nm)/Au (1.0 nm)/Ag (10 nm). In order to improve the calculating efficiency, only one simulation unit including one nanohole was simulated. 3731 different combinations of the pitch size and nanohole depth of the 2-D photonic-structured AR coatings were calculated for maximizing J_{SC} . All simulations were operated on a server (Intel(R) Xeon(R) Silver 4216 CPU @ 2.10 GHz, 256 GB).

Fabrication of Photonic-Structured AR Coating: The photonic-structured Si mould was prepared using a 375 μ m thick p-type Si (100) substrate, with a resistivity of ≈ 10 Ω cm, cleaned using piranha solution and deionized water. Monodisperse polystyrene (PS) nanoparticles were assembled into a close packed monolayer on Si substrate using the Langmuir-Blodgett technique, acting as the mask. The size and spacing of the nanoparticles were tuned by an isotropic reactive ion etching (RIE) using a gas mixture of CHF₃ and O₂, operated under a power of 100 W and a pressure of 250 mTorr. Si nanopillars were then formed by Cl₂-based anisotropic RIE using a power of 40 W and a pressure of 10 mTorr. PS nanoparticles at the top of nanopillars were re-

moved by ultrasonic to form the desired photonic-structured Si mould. PDMS solution, formulated using a mixture of the curing agent and base resin with a weight ratio of curing agent to base resin of 1:10, was poured directly onto the photonic-structured Si mould and cured at 70 °C for 2 h. A $\approx 150\ \mu\text{m}$ thick cured inverted 2-D photonic-structured PDMS AR coating was carefully peeled off from the Si mould and attached to the front glass side of the ST-OSCs, with the photonic-structured PDMS AR coating facing to the incident light.

Devices Fabrication: The ITO/glass substrates with a sheet resistance of $15\ \Omega\ \text{sq}^{-1}$ were cleaned by ultrasonication sequentially with detergent, deionized water, acetone, and isopropyl alcohol each for 30 min. After the wet cleaning, the ITO/glass substrates were exposed to the ultraviolet treatment in ozone for 15 min prior to the device fabrication. A 40 nm-thick PEDOT:PSS-Nb₂C hybrid HTL was deposited on the ITO/glass substrates using spin-coating at a rotation speed of 3000 rpm for 60 s, followed by an annealing at 130 °C for 20 min in air. The PM6:BTP-eC9:L8-BO mixture solutions having a concentration of 16 mg mL⁻¹ but with different weight ratios of PM6 to BTP-eC9 to L8-BO, dissolved in chloroform solvent with a 0.5% of 1,8-diiodooctane (DIO) additive, were prepared for preparation of the ternary active layer. PM6:BTP-eC9:L8-BO BHJ active layers were deposited on the PEDOT:PSS-Nb₂C hybrid HTL using spin-coating method. The thickness of the active layers was controlled by the rotation speed over the range from 4000 to 7000 rpm for 30 s, followed by an annealing at 100 °C for 10 min in the glove box with O₂ and H₂O levels < 0.1 ppm. An 8.0 nm-thick BCP ETL was deposited on the BHJ by thermal evaporation. A bilayer Au (1.0 nm)/Ag (10 nm) upper contact was deposited by thermal evaporation. A double layer OCL of Na₃AlF₆ (170 nm)/ZnS (110 nm) was deposited on the Au (1.0 nm)/Ag (10 nm) using thermal evaporation. The ST-OSCs had an active area of 5.0 mm², defined by the overlap area between the front ITO contact and the rear metal electrode.

Material and Device Characterizations: ZnS was purchased from Adamas. Na₃AlF₆ was purchased from Macklin. PDMS and curing agent were purchased from Shanghai Deji Co., Ltd. PEDOT:PSS solution (Clevios P VP 4083) was purchased from Heraeus. PM6, BTP-eC9, and L8-BO were purchased from Organtec Ltd. Chloroform and DIO were purchased from Sigma Aldrich. All chemicals and reagents were used as received without further purification.

The transmission and absorption spectra of the photoactive layers were measured using a UV-vis spectrophotometer (Jasco V-750). The surface morphologies of the BHJ films with different ratios of PM6 to BTP-eC9 to L8-BO were analyzed using AFM (Nanonavi SPA-400SPM). The TEM images of the BHJ films were obtained by using a Themis ETEM G3 microscope. The surface morphology of the 2-D photonic-structured PDMS AR coatings were analyzed using SEM (HITACHI S-4800). The wavelength-dependent refractive indices and extinction coefficients of the functional layers used in the simulation were measured using VASE (J.A. Woollam RC2-XI).

J-V characteristics of the ST-OSCs were measured using a calibrated AM1.5G solar simulator (Newport Oriel Sol3A) (100 mW cm⁻²) and a source meter (Keithley 2420). EQE spectra of the OSCs were measured using a 7-SCSpec solar cell measurement system (7-STAR Co.). The stability of the as-prepared

ST-OSCs was monitored in the N₂-purged glove box with O₂ and H₂O levels below 0.1 ppm, at room temperature.

Supporting Information

Supporting Information is available from the Wiley Online Library or from the author.

Acknowledgements

This work was financially supported by National Natural Science Foundation of China (12174244). S.W. acknowledges the funding support from the Program for Professor of Special Appointment (Eastern Scholar) at the Shanghai Institutions of Higher Learning and the Shanghai Rising-Star Program (19QA1403800). F.Z. is thankful for the financial support by the Research Grants Council, Hong Kong Special Administrative Region, China (12302419, C5037-18GF, and N_HKBU201/19), SZ-HK-Macau Science and Technology Plan Project (SGDX20201103095400005), and Guangdong Basic and Applied Basic Research Fund GDSTC (2022A1515010020).

Conflict of Interest

The authors declare no conflict of interest.

Data Availability Statement

The data that support the findings of this study are available from the corresponding author upon reasonable request.

Keywords

2D photonic structures, high-throughput optical screening, NIR absorption enhancement, semitransparent organic solar cells, ternary blend systems

Received: May 6, 2023

Revised: June 22, 2023

Published online:

- [1] C. Sun, R. Xia, H. Shi, H. Yao, X. Liu, J. Hou, F. Huang, H.-L. Yip, Y. Cao, *Joule* **2018**, *2*, 1816.
- [2] Y. Li, X. Guo, Z. Peng, B. Qu, H. Yan, H. Ade, M. Zhang, S. R. Forrest, *Proc. Natl. Acad. Sci. U.S.A.* **2020**, *117*, 21147.
- [3] C. Ballif, L.-E. Perret-Aebi, S. Lufkin, E. Rey, *Nat. Energy* **2018**, *3*, 438.
- [4] S.-Y. Chang, P. Cheng, G. Li, Y. Yang, *Joule* **2018**, *2*, 1039.
- [5] S. Guan, Y. Li, K. Yan, W. Fu, L. Zuo, H. Chen, *Adv. Mater.* **2022**, *34*, 2205844.
- [6] J. Yuan, Y. Zhang, L. Zhou, G. Zhang, H.-L. Yip, T.-K. Lau, X. Lu, C. Zhu, H. Peng, P. A. Johnson, M. Leclerc, Y. Cao, J. Ulanski, Y. Li, Y. Zou, *Joule* **2019**, *3*, 1140.
- [7] P. Cheng, H. Wang, Y. Zhu, R. Zheng, T. Li, C. Chen, T. Huang, Y. Zhao, R. Wang, D. Meng, Y. Li, C. Zhu, K. Wei, X. Zhan, Y. Yang, *Adv. Mater.* **2020**, *32*, 2003891.
- [8] S. Y. Park, C. Labanti, J. Luke, Y. Chin, J. Kim, *Adv. Energy Mater.* **2022**, *12*, 2103237.
- [9] D. Wang, H. Liu, Y. Li, G. Zhou, L. Zhan, H. Zhu, X. Lu, H. Chen, C.-Z. Li, *Joule* **2021**, *5*, 945.

- [10] E. Pascual-San-José, G. Sadoughi, L. Lucera, M. Stella, E. Martínez-Ferrero, G. E. Morse, M. Campoy-Quiles, I. Burgués-Ceballos, J. Mater. Chem. A **2020**, *8*, 9882.
- [11] L. Zhu, M. Zhang, J. Xu, C. Li, J. Yan, G. Zhou, W. Zhong, T. Hao, J. Song, X. Xue, Z. Zhou, R. Zeng, H. Zhu, C.-C. Chen, R. C. I. MacKenzie, Y. Zou, J. Nelson, Y. Zhang, Y. Sun, F. Liu, Nat. Mater. **2022**, *21*, 656.
- [12] Y. Wei, Z. Chen, G. Lu, N. Yu, C. Li, J. Gao, X. Gu, X. Hao, G. Lu, Z. Tang, J. Zhang, Z. Wei, X. Zhang, H. Huang, Adv. Mater. **2022**, *34*, 2204718.
- [13] W. Gao, F. Qi, Z. Peng, F. R. Lin, K. Jiang, C. Zhong, W. Kaminsky, Z. Guan, C. Lee, T. J. Marks, H. Ade, A. K.-Y. Jen, Adv. Mater. **2022**, *34*, 2202089.
- [14] Y. Cui, Y. Xu, H. Yao, P. Bi, L. Hong, J. Zhang, Y. Zu, T. Zhang, J. Qin, J. Ren, Z. Chen, C. He, X. Hao, Z. Wei, J. Hou, Adv. Mater. **2021**, *33*, 2102420.
- [15] W. Lan, J. Gu, S. Wu, Y. Peng, M. Zhao, Y. Liao, T. Xu, B. Wei, L. Ding, F. Zhu, EcoMat **2021**, *3*, e12134.
- [16] T. Xu, C. Gong, S. Wang, H. Lian, W. Lan, G. Lévêque, B. Grandidier, J. Plain, R. Bachelot, B. Wei, F. Zhu, Sol. RRL **2020**, *4*, 1900522.
- [17] N. Zhang, T. Jiang, C. Guo, L. Qiao, Q. Ji, L. Yin, L. Yu, P. Murto, X. Xu, Nano Energy **2020**, *77*, 105111.
- [18] P. Yin, Z. Yin, Y. Ma, Q. Zheng, Energy Environ. Sci. **2020**, *13*, 5177.
- [19] Z. Hu, J. Wang, X. Ma, J. Gao, C. Xu, X. Wang, X. Zhang, Z. Wang, F. Zhang, J. Mater. Chem. A **2021**, *9*, 6797.
- [20] Y. Zhang, J. Zheng, Z. Jiang, X. He, J. Kim, L. Xu, M. Qin, X. Lu, A. K. K. Kyaw, W. C. H. Choy, Adv. Energy Mater. **2023**, *13*, 2203266.
- [21] X. Liu, Z. Zhong, R. Zhu, J. Yu, G. Li, Joule **2022**, *6*, 1918.
- [22] X. Huang, Y. Cheng, Y. Fang, L. Zhang, X. Hu, S. Y. Jeong, H. Zhang, H. Y. Woo, F. Wu, L. Chen, Energy Environ. Sci. **2022**, *15*, 4776.
- [23] W. Liu, S. Sun, L. Zhou, Y. Cui, W. Zhang, J. Hou, F. Liu, S. Xu, X. Zhu, Angew. Chem., Int. Ed. **2022**, *61*, e202116111.
- [24] W. Liu, S. Sun, S. Xu, H. Zhang, Y. Zheng, Z. Wei, X. Zhu, Adv. Mater. **2022**, *34*, 2200337.
- [25] D. Wang, R. Qin, G. Zhou, X. Li, R. Xia, Y. Li, L. Zhan, H. Zhu, X. Lu, H. Yip, H. Chen, C. Li, Adv. Mater. **2020**, *32*, 2001621.
- [26] N. Schopp, G. Akhtanova, P. Panoy, A. Arbut, S. Chae, A. Yi, H. J. Kim, V. Promarak, T. Nguyen, V. V. Brus, Adv. Mater. **2022**, *34*, 2203796.
- [27] Z. Liao, D. Hu, H. Tang, P. Huang, R. Singh, S. Chung, K. Cho, M. Kumar, L. Hou, Q. Chen, W. Yu, H. Chen, K. Yang, Z. Kan, F. Liu, Z. Xiao, G. Li, S. Lu, J. Mater. Chem. A **2022**, *10*, 7878.
- [28] Y. Cai, Y. Li, R. Wang, H. Wu, Z. Chen, J. Zhang, Z. Ma, X. Hao, Y. Zhao, C. Zhang, F. Huang, Y. Sun, Adv. Mater. **2021**, *33*, 2101733.
- [29] X. Huang, L. Zhang, Y. Cheng, J. Oh, C. Li, B. Huang, L. Zhao, J. Deng, Y. Zhang, Z. Liu, F. Wu, X. Hu, C. Yang, L. Chen, Y. Chen, Adv. Funct. Mater. **2022**, *32*, 2108634.
- [30] L. Zhao, X. Huang, Y. Wang, S. Y. Jeong, B. Huang, J. Deng, J. Liu, Y. Cheng, H. Y. Woo, F. Wu, L. Chen, L. Chen, Chem. Eng. J. **2023**, *451*, 139081.
- [31] X. Wu, S. Liu, H. Li, X. Meng, X. Hu, R. Guo, Y. Chen, Adv. Opt. Mater. **2022**, *10*, 2201803.
- [32] X. Li, R. Xia, K. Yan, J. Ren, H.-L. Yip, C.-Z. Li, H. Chen, ACS Energy Lett. **2020**, *5*, 3115.
- [33] Y. Bai, F. Han, R. Shi, F. Wang, S. Jiang, J. Wang, Z. Tan, Sol. RRL **2022**, *6*, 2200174.
- [34] Y. Li, C. Ji, Y. Qu, X. Huang, S. Hou, C. Li, L. Liao, L. J. Guo, S. R. Forrest, Adv. Mater. **2019**, *31*, 1903173.
- [35] J. Zhang, G. Xu, F. Tao, G. Zeng, M. Zhang, Y. M. Yang, Y. Li, Y. Li, Adv. Mater. **2019**, *31*, 1807159.
- [36] J. W. Leem, S. Kim, S. H. Lee, J. A. Rogers, E. Kim, J. S. Yu, Adv. Energy Mater. **2014**, *4*, 1301315.
- [37] W. Lan, Y. Wang, J. Singh, F. Zhu, ACS Photonics **2018**, *5*, 1144.
- [38] X. Yuan, R. Sun, Y. Wu, T. Wang, Y. Wang, W. Wang, Y. Yu, J. Guo, Q. Wu, J. Min, Adv. Funct. Mater. **2022**, *32*, 2200107.
- [39] R. Xia, C. J. Brabec, H.-L. Yip, Y. Cao, Joule **2019**, *3*, 2241.
- [40] T. Xu, Y. Luo, S. Wu, B. Deng, S. Chen, Y. Zhong, S. Wang, G. Lévêque, R. Bachelot, F. Zhu, Adv. Sci. **2022**, *9*, 2202150.
- [41] B. Deng, H. Lian, B. Xue, R. Song, S. Chen, Z. Wang, T. Xu, H. Dong, S. Wang, Small **2023**, *19*, 2207505.
- [42] H. R. Yeom, S. Song, S. Y. Park, H. S. Ryu, J. W. Kim, J. Heo, H. W. Cho, B. Walker, S.-J. Ko, H. Y. Woo, J. Y. Kim, Nano Energy **2020**, *77*, 105146.
- [43] Z. Hu, J. Wang, Z. Wang, W. Gao, Q. An, M. Zhang, X. Ma, J. Wang, J. Miao, C. Yang, F. Zhang, Nano Energy **2019**, *55*, 424.
- [44] J. Mao, J. Iocozzia, J. Huang, K. Meng, Y. Lai, Z. Lin, Energy Environ. Sci. **2018**, *11*, 772.
- [45] J. Jing, S. Dong, K. Zhang, Z. Zhou, Q. Xue, Y. Song, Z. Du, M. Ren, F. Huang, Adv. Energy Mater. **2022**, *12*, 2200453.
- [46] C. Yang, D. Liu, M. Bates, M. C. Barr, R. R. Lunt, Joule **2019**, *3*, 1803.
- [47] B. Deng, Y. Shen, K. Zheng, C. Wang, G. Lévêque, T. Xu, Sol. RRL **2023**, *2300211*.
- [48] O. I. Elmi, O. Cristini-Robbe, M. Y. Chen, B. Wei, R. Bernard, D. Yarekha, E. Okada, S. Ouendi, X. Portier, F. Gourbilleau, T. Xu, D. Stiévenard, Nanotechnology **2018**, *29*, 285403.
- [49] T. Xu, Z. Tian, O. I. Elmi, C. Krzeminski, O. Robbe, Y. Lambert, D. Yakeda, E. Okada, B. Wei, D. Stiévenard, Physica E **2017**, *93*, 190.
- [50] D. Zhou, Y. Pennec, B. Djafari-Rouhani, O. Cristini-Robbe, T. Xu, Y. Lambert, Y. Deblock, M. Faucher, D. Stiévenard, J. Appl. Phys. **2014**, *115*, 134304.